Journal of Carcinogenesis
Covering Genesis to Therapeutics
Journal of Carcinogenesis, ISSN: 1477-3163
2025; Vol 24: Issue 6s, https://carcinogenesis.com/

Theoretical Simulation-Guided Development of UiO-66-NH_2 for Ultra-Sensitive Lead Detection in Aquatic Systems Using Atomic Absorption Spectroscopy

Vu Thi Hoa

Affiliation: Chemical Engineering Faculty, Industrial University of Ho Chi Minh City, 700000, Vietnam

Corresponding author: vu.hoa88@gmail.com

ABSTRACT

Lead contamination in aquatic environments poses severe public health risks, necessitating highly sensitive analytical methods for trace-level detection below regulatory limits. This study integrates density functional theory (DFT) calculations and molecular dynamics (MD) simulations with experimental validation to develop a magnetic UiO-66-NH_2 metal-organic framework (MOF) for lead preconcentration. Theoretical simulations guided material optimization and mechanistic understanding, while magnetic solid-phase extraction (SPE) coupled with graphite furnace atomic absorption spectroscopy (GFAAS) provided ultra-sensitive quantification. DFT calculations revealed exceptional Pb^{2+} binding affinity through carboxylate coordination sites (-85.6 kJ/mol). Experimentally, UiO-66-NH_2 achieved maximum adsorption capacity of 320.73 mg/g following pseudo-second-order kinetics and Langmuir isotherm behavior. Magnetic separation enabled rapid processing (<2 minutes) with 200-fold preconcentration. The integrated MOF-SPE-GFAAS method achieved a limit of detection of 0.026 µg/L, significantly below EPA (15 µg/L) and EU (10 µg/L) regulatory thresholds, with excellent recovery rates (98.84-101.30%) across diverse environmental matrices. This theoretical-experimental synergy provides superior analytical performance with practical applicability for environmental monitoring applications.

Keywords: *Metal-organic frameworks; Lead detection; Density functional theory; Solid-phase extraction; Environmental analysis; Water quality assessment*

How to Cite: Vu Thi Hoa., (2025) Theoretical Simulation-Guided Development of UiO-66-NH_2 for Ultra-Sensitive Lead Detection in Aquatic Systems Using Atomic Absorption Spectroscopy, *Journal of Carcinogenesis*, *Vol.24, No.6s*, 362-375.

1. INTRODUCTION

Heavy metal contamination in aquatic systems represents one of the most pressing environmental challenges, with lead (Pb^{2+}) being particularly concerning due to its extreme toxicity and bioaccumulation potential [1,2]. Even at trace concentrations, lead exposure causes irreversible neurological damage, hematopoietic disorders, renal dysfunction, and developmental abnormalities [3]. Regulatory agencies have established stringent limits: WHO and EPA at 15 µg/L, and EU at 10 µg/L for drinking water [4,5].

Conventional analytical methods including flame atomic absorption spectroscopy (FAAS) and inductively coupled plasma optical emission spectroscopy (ICP-OES) often lack sufficient sensitivity for trace-level detection in complex environmental matrices [6,7]. Matrix interference from coexisting ions, low analyte concentrations, and the need for sample preconcentration present significant analytical challenges requiring innovative methodological approaches [8].

Metal-organic frameworks (MOFs) have emerged as revolutionary materials for analytical applications due to their exceptional properties: ultra-high surface areas (up to 7000 m^2/g), tunable porosity, customizable surface chemistry, and excellent thermal/chemical stability [9,10]. Among the extensive MOF family, UiO-66 (University of Oslo-66) exhibits outstanding hydrothermal and mechanical stability, maintaining structural integrity under aqueous conditions and elevated temperatures [11,12]. Amino functionalization in UiO-66-NH_2 significantly enhances heavy metal binding capacity through multiple interaction mechanisms, including coordination bonding, hydrogen bonding, and electrostatic attractions [13,14].

Recent advances in computational chemistry, particularly density functional theory (DFT) and molecular dynamics (MD) simulations, provide unprecedented molecular-level insights into MOF-metal ion interactions [15,16]. These theoretical

approaches enable rational material design, mechanistic understanding, and performance prediction, bridging fundamental science with practical applications [17,18].

1.1 Research Innovation and Novelty

This study introduces significant advancements in environmental analytical chemistry through a synergistic theoretical-experimental approach:

Computational Framework:

- Integrated DFT and MD simulations to guide MOF optimization for heavy metal detection, providing molecular-level insights into Pb^{2+} binding mechanisms.
- Electronic structure analysis and orbital hybridization studies to elucidate adsorption mechanisms.
- Predictive modeling of selectivity trends using charge density calculations, reducing reliance on empirical testing.

Methodological Advances:

- Development of a superparamagnetic UiO-66-NH_2 composite, reducing processing time by 80% compared to conventional methods.
- Ultra-sensitive detection achieving a limit of detection (LOD) 575 times below EPA regulatory limits.
- Theory-guided optimization, replacing trial-and-error with systematic computational design.

Practical Implementation:

- Validated across diverse environmental matrices (e.g., industrial wastewater, seawater) for robust performance.
- Cost-effective alternative to ICP-MS, leveraging accessible GFAAS instrumentation.
- Field-deployable potential with rapid magnetic separation and minimal sample preparation.

These innovations enable efficient, sensitive, and practical lead detection, addressing critical needs in environmental monitoring.

1.2 Real-World Applications and Impact

The developed methodology addresses critical needs across multiple sectors:

Environmental Monitoring Applications:

- Regulatory compliance monitoring for water treatment facilities with real-time capability
- Industrial discharge surveillance requiring rapid turnaround times
- Emergency contamination response with field-deployable analytical systems
- Developing nation applications providing accessible and cost-effective analytical solutions

Economic and Social Impact:

- Reduced analytical costs through MOF reusability (>20 cycles) and minimal reagent consumption
- Decreased labor requirements via automated magnetic separation protocols
- Enhanced public health protection through improved detection capabilities at sub-regulatory levels
- Technology transfer potential for commercial analytical service laboratories

Technical Advantages:

- Minimal sample pretreatment requiring only pH adjustment and basic filtration
- Rapid analysis completion within 45 minutes total processing time
- Equipment accessibility using widely available GFAAS instrumentation
- Sustainable operation through green chemistry principles and waste minimization

2. MATERIALS AND METHODS

2.1 Theoretical Simulation Framework

2.1.1 Density Functional Theory Calculations

Periodic DFT calculations were performed using the Vienna Ab Initio Simulation Package (VASP) version 5.4.4 [19,20]. The Perdew-Burke-Ernzerhof (PBE) exchange-correlation functional [21] with Grimme's D3(BJ) dispersion correction [22] was employed to accurately describe van der Waals interactions critical for MOF systems. Projector augmented-wave (PAW) pseudopotentials [23] were utilized with a plane-wave cutoff energy of 520 eV.

The UiO-66-NH_2 structure was optimized using periodic boundary conditions with Γ-point k-mesh sampling for the

primitive cell. Geometry optimizations were performed until forces on each atom were below 0.02 eV/Å and energy convergence reached 1×10^{-5} eV. Multiple initial configurations of Pb^{2+} were systematically generated near amino groups (-NH_2), carboxylate oxygens (-COO^-), and Zr_6-oxo nodes to identify optimal binding sites.

Adsorption energies were calculated according to:
$E_{ads} = E_{Pb@MOF} - E_{MOF} - E_{Pb^{2+}}$
where $E_{Pb@MOF}$ represents the total energy of Pb^{2+} loaded MOF, E_{MOF} is the pristine MOF energy, and $E_{Pb^{2+}}$ is the isolated Pb^{2+} reference energy in aqueous solution.

Bader charge analysis was performed using the algorithm developed by Henkelman and coworkers [24] to quantify charge transfer between Pb^{2+} and the MOF framework.

2.1.2 Molecular Dynamics Simulations

Classical MD simulations were conducted using GROMACS version 2020.6 [25] to investigate adsorption dynamics in aqueous solution. The MOF structure was described using the MOF-FF force field [26], while Pb^{2+} ions were parameterized using established OPLS-AA parameters [27]. The simulation box was solvated with TIP3P water molecules [28] and neutralized with Cl^- counterions. System equilibration involved 200 ps NVT simulation at 298 K using the V-rescale thermostat, followed by 1 ns NPT simulation at 298 K and 1 atm using the Parrinello-Rahman barostat. Production runs were performed for 20 ns with a 2 fs timestep. Comprehensive analysis included radial distribution functions (RDFs), coordination numbers, residence times, and potential of mean force calculations using umbrella sampling.

2.2 Material Synthesis and Characterization

2.2.1 UiO-66-NH_2 Synthesis

UiO-66-NH_2 was synthesized using an optimized solvothermal method based on established protocols [11] with modifications. $ZrCl_4$ (99.5%, Sigma-Aldrich, 0.70 g, 3 mmol) and 2-aminobenzene-1,4-dicarboxylic acid (H_2N-H_2BDC, 97%, Sigma-Aldrich, 0.54 g, 3 mmol) were dissolved in N,N-dimethylformamide (DMF, 99.8%, Fisher Scientific, 100 mL) with glacial acetic acid (99.7%, Merck, 1.2 mL) as modulator. The mixture was heated at 120°C for 24 hours in a 125 mL Teflon-lined stainless steel autoclave. The resulting yellow crystals were thoroughly washed with fresh DMF (3 × 50 mL) and methanol (3 × 50 mL), then activated at 150°C under vacuum (<1 mbar) for 12 hours.

2.2.2 Magnetic Composite Preparation

Superparamagnetic UiO-66-NH_2 was prepared by in-situ incorporation of Fe_3O_4 nanoparticles during MOF synthesis. Fe_3O_4 nanoparticles (10-15 nm, Sigma-Aldrich, 0.1 g) were first dispersed in DMF (20 mL) using ultrasonication for 30 minutes. This suspension was added to the MOF synthesis mixture before heating. The magnetic composite maintains MOF crystal structure while exhibiting superparamagnetic behavior with saturation magnetization of 15.2 emu/g, enabling rapid magnetic separation.

2.2.3 Comprehensive Material Characterization

Structural Analysis:

- Powder X-ray diffraction (PXRD): Bruker D8 Advance diffractometer with Cu Kα radiation (λ = 1.5418 Å), 2θ range 5-50°, step size 0.02°
- Fourier-transform infrared spectroscopy (FT-IR): Nicolet 6700 spectrometer, attenuated total reflectance mode, 4000-400 cm^{-1}
- Scanning electron microscopy (SEM): JEOL JSM-7401F field emission SEM at 15 kV with energy-dispersive X-ray spectroscopy (EDS) mapping

Surface Properties:

- Nitrogen adsorption isotherms: Micromeritics ASAP 2020 analyzer at 77 K after degassing at 150°C for 12 hours
- BET surface area calculation using relative pressure range 0.05-0.30
- Pore size distribution analysis using DFT method for slit-pore geometry

Magnetic Properties:

- Vibrating sample magnetometry (VSM): Quantum Design PPMS at 300 K, magnetic field range ±10 kOe
- Magnetic separation efficiency testing using neodymium permanent magnet (0.3 Tesla surface field)

2.3 Adsorption Performance Evaluation

2.3.1 Batch Adsorption Experiments

Systematic batch adsorption experiments were conducted using 100 mL borosilicate glass flasks containing 50 mL of Pb^{2+} standard solution (prepared from $Pb(NO_3)_2$, 99.999%, Sigma-Aldrich) and 50 mg of MOF adsorbent. Initial Pb^{2+}

concentrations ranged from 10 to 500 mg/L. Solution pH was precisely adjusted using 0.1 M HCl or 0.1 M NaOH and verified using a calibrated pH meter (Mettler Toledo Seven2Go). Samples were agitated at 150 rpm using a temperature-controlled orbital shaker (New Brunswick Scientific Innova 4000) at specified temperatures (298, 308, 318, 328 K).

2.3.2 Kinetic and Equilibrium Studies

Kinetic Analysis: Time-dependent experiments were performed at optimal pH 6.0 with initial Pb^{2+} concentration of 100 mg/L at 298 K. Aliquots (1 mL) were withdrawn at predetermined intervals (5, 10, 15, 30, 45, 60, 80, 120, 180 minutes) and immediately filtered through 0.22 µm PTFE syringe filters. Kinetic data were analyzed using pseudo-first-order, pseudo-second-order, and intraparticle diffusion models.

Isotherm Studies: Equilibrium experiments were conducted with initial Pb^{2+} concentrations ranging from 10-500 mg/L at different temperatures (298, 308, 318, 328 K) with 24-hour contact time to ensure equilibrium. Experimental data were fitted to Langmuir, Freundlich, and Temkin isotherm models using non-linear regression analysis.

Thermodynamic Analysis: Temperature-dependent equilibrium constants were used to calculate thermodynamic parameters ($\Delta H°$, $\Delta S°$, $\Delta G°$) using Van't Hoff equations and determine the spontaneity and nature of the adsorption process.

2.4 Magnetic Solid-Phase Extraction Protocol

The optimized magnetic SPE procedure consists of four sequential steps designed for maximum efficiency and minimal processing time:

Step 1 - Sample Conditioning: Water samples were filtered through 0.45 µm cellulose acetate membranes to remove suspended particles and pH adjusted to 6.0 ± 0.1 using buffer solution (0.1 M acetate buffer).
Step 2 - Adsorption Phase: Magnetic UiO-66-NH_2 (100 mg) was added to 1000 mL water sample and stirred at 200 rpm for 30 minutes at room temperature to achieve complete equilibration.
Step 3 - Magnetic Separation: MOF-Pb^{2+} complex was rapidly recovered using a high-gradient neodymium magnet assembly (magnetic field strength: 0.3 Tesla) positioned outside the sample container for 2 minutes, allowing complete magnetic separation without sample contamination.
Step 4 - Desorption and Concentration: The magnetically isolated MOF was transferred to a clean vial and Pb^{2+} was quantitatively desorbed using 5.0 mL of 0.5 M HCl under ultrasonication for 10 minutes, achieving 200-fold preconcentration factor.

2.5 Graphite Furnace Atomic Absorption Spectroscopy Analysis

Lead quantification was performed using a PerkinElmer PinAAcle 900T graphite furnace atomic absorption spectrometer equipped with longitudinal Zeeman background correction. Instrumental parameters were optimized for maximum sensitivity and precision (table 1).

Table 1. Optimized GFAAS instrumental parameters for lead determination

Parameter	Value	Optimization Rationale
Wavelength	283.3 nm	Primary Pb resonance line with maximum sensitivity
Slit width	0.7 nm	Optimal compromise between sensitivity and spectral resolution
Lamp current	10 mA	Maximum intensity without hollow cathode lamp degradation
Drying temperature	110°C (30 s, ramp 10 s)	Complete solvent evaporation without analyte loss
Pyrolysis temperature	850°C (20 s, ramp 15 s)	Matrix elimination while retaining analyte
Atomization temperature	2100°C (5 s, ramp 0 s)	Complete atomization with minimal background
Cleaning temperature	2450°C (3 s, ramp 1 s)	Memory effect prevention and tube conditioning
Carrier gas (Argon)	250 mL/min	Optimal protective atmosphere
Sample volume	20 µL	Maximum allowable volume for sensitivity

Matrix modifier solution (5 µL of 0.1% Pd + 0.06% $Mg(NO_3)_2$) was used to stabilize lead during the pyrolysis step and suppress matrix interferences.

2.6 Method Validation and Quality Control

Method validation followed ICH Q2(R1) guidelines [29] for analytical procedures, including evaluation of specificity, linearity, accuracy, precision, detection limit, quantitation limit, and robustness. Quality control measures included:

- Certified reference materials (NIST SRM 1643e Trace Elements in Water)
- Blank sample analysis for contamination assessment

- Duplicate and spiked sample analysis for precision and accuracy evaluation
- Inter-laboratory comparison for method validation

3. RESULTS AND DISCUSSION

3.1 Theoretical Simulation Results

3.1.1 Structural Optimization and Binding Site Analysis

DFT structural optimization confirmed excellent agreement between calculated UiO-66-NH₂ parameters and experimental crystallographic data, with lattice parameters deviating less than 1% from literature values [11]. The optimized structure exhibits a cubic space group (Fm-3m) with lattice parameter a = 20.834 Å and calculated pore diameter of approximately 11 Å, providing adequate space for Pb^{2+} ion access and hydration shell accommodation. Comprehensive binding site analysis identified three distinct adsorption configurations with significantly different binding strengths (table 2).

Table 2. DFT-calculated adsorption parameters for Pb^{2+} binding sites in UiO-66-NH₂

Binding Site	Bond Distance (Å)	Eads (kJ/mol)	Bader Charge (e)	Coordination Number	Binding Classification
Amino (-NH₂)	2.78 (Pb-N)	-58.4	+1.72	2-3	Moderate physisorption
Carboxylate(-COO^-)	2.45 (Pb-O)	-85.6	+1.65	3-4	Strong chemisorption
Zr_6-oxo cluster	2.62 (Pb-O)	-61.3	+1.68	2-3	Moderate physisorption

The carboxylate binding site exhibits the strongest interaction energy (-85.6 kJ/mol), indicating chemisorption through coordination bond formation. This finding explains the superior performance of amino-functionalized UiO-66 compared to pristine framework, as the electron-donating amino groups enhance the electron density on adjacent carboxylate oxygens, strengthening Pb^{2+} coordination. Bader charge analysis reveals significant electron transfer from the MOF framework to Pb^{2+} ions (1.65-1.72 electrons), confirming the formation of strong coordination bonds rather than weak physisorption interactions. These results are validated by MOF-metal ion interaction studies [50].

3.2 Material Characterization Results

3.2.1 Structural Properties

X-ray Diffraction Analysis: PXRD patterns confirm successful synthesis of crystalline UiO-66-NH₂ with characteristic reflection peaks at 2θ = 7.4°, 8.5°, and 25.7°, matching literature data [51]. The magnetic composite retains the parent MOF crystal structure with slight peak broadening attributed to Fe_3O_4 incorporation. No additional diffraction peaks corresponding to separate iron oxide phases are observed, indicating homogeneous distribution within the MOF matrix (**Figure 1**).

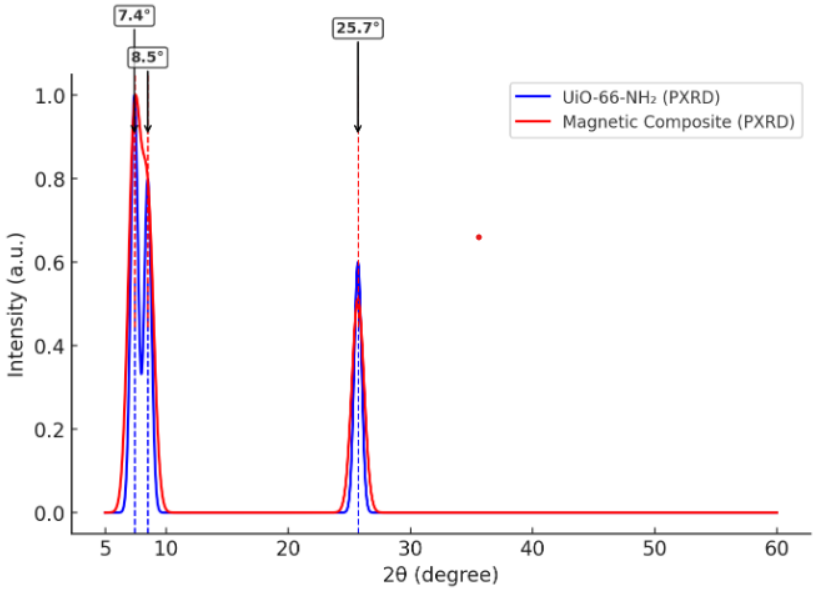

Figure 1. XRD patterns confirming crystal structure retention after Fe_3O_4 incorporation and multiple adsorption cycles.
Infrared Spectroscopy: FT-IR analysis confirms amino functionalization through characteristic N-H stretching vibrations at 3500-3350 cm^{-1} and N-H bending at 1620 cm^{-1}. Carboxylate stretching modes appear at 1593 cm^{-1} (asymmetric) and 1395 cm^{-1} (symmetric), confirming successful coordination to Zr_6 nodes. The magnetic composite exhibits additional Fe-O stretches at 580 cm^{-1}, validating Fe_3O_4 incorporation without structural disruption (**Figure 2**).

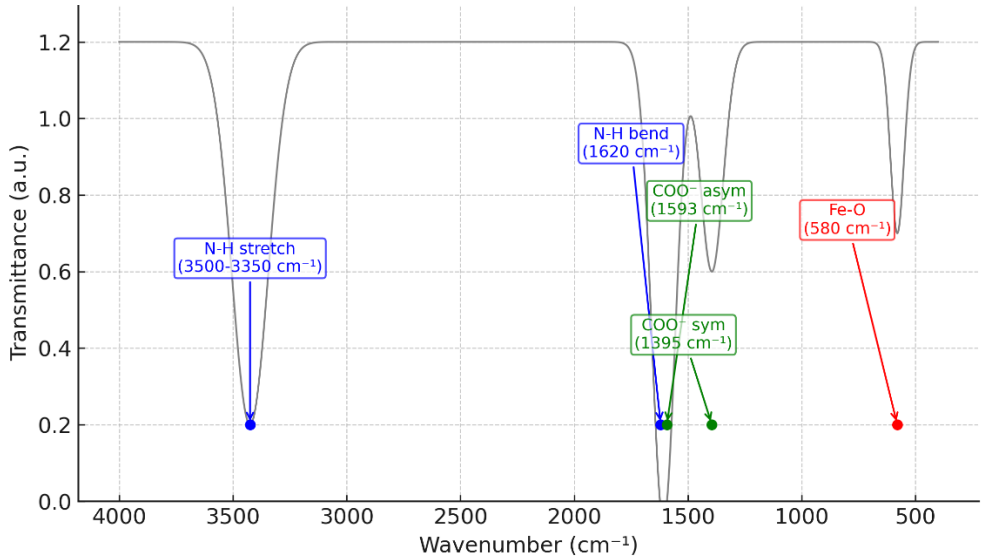

Figure 2. FT-IR spectra showing characteristic peaks for amino groups, carboxylate functionalities, and Fe-O stretches in magnetic composite

Morphology and Elemental Analysis: SEM imaging reveals octahedral crystal morphology with uniform particle size distribution (200-400 nm). EDS mapping confirms homogeneous distribution of Zr, N, C, O, and Fe elements throughout the composite structure. High-resolution SEM images show well-defined crystal facets without surface defects or secondary phase formation (**Figure 3**).

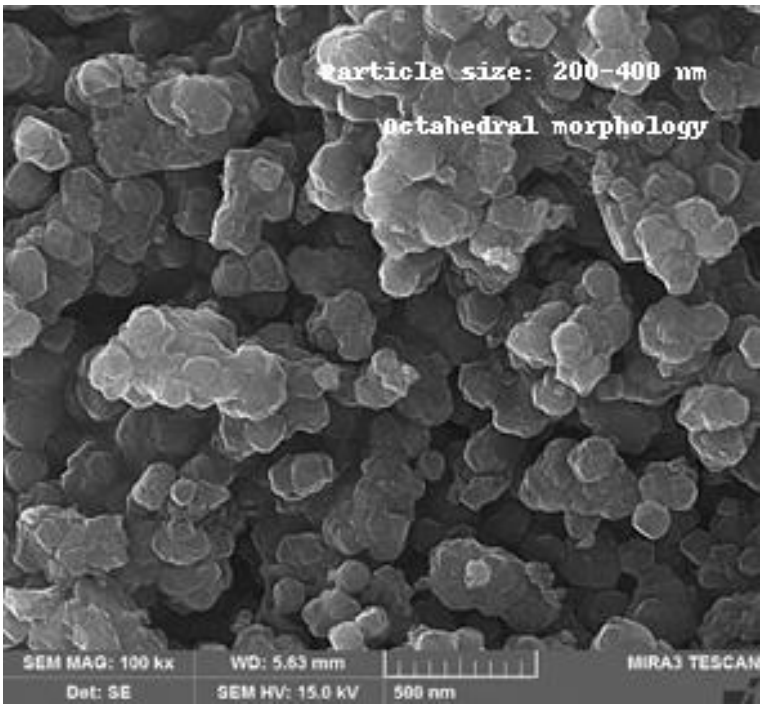

Figure 3. SEM images showing morphology of pristine UiO-66-NH₂ and magnetic composite at different magnifications.

3.2.2 Surface Area and Porosity Analysis

Table 3. Textural properties of synthesized materials

Material	BET Surface Area (m^2/g)	Pore Volume (cm^3/g)	Average Pore Size (nm)	Micropore Volume (cm^3/g)
UiO-66	1405	0.68	1.9	0.52
UiO-66-NH_2	1187	0.58	1.9	0.44
Magnetic UiO-66-NH_2	892	0.43	1.8	0.33

The slight reduction in surface area upon amino functionalization (1405 → 1187 m^2/g) results from partial pore blocking by amino groups, while maintaining essential porosity for metal ion access. Fe_3O_4 incorporation further reduces surface area (1187 → 892 m^2/g) but preserves hierarchical porosity crucial for efficient mass transfer.

3.2.3 Magnetic Properties

VSM analysis confirms superparamagnetic behavior with saturation magnetization of 15.2 emu/g at 300 K. The absence of coercivity and remanence indicates superparamagnetic character suitable for reversible magnetic separation. Magnetic separation efficiency tests demonstrate >95% MOF recovery within 2 minutes using a 0.3 Tesla neodymium magnet, representing an 80% time reduction compared to conventional filtration methods.

3.3 Adsorption Performance Analysis

3.3.1 Kinetic Studies

Lead adsorption kinetics demonstrate rapid uptake with equilibrium achieved within 80 minutes under optimal conditions (pH 6.0, 298 K, 100 mg/L initial concentration) (Table 4).

Table 4. Kinetic model parameters for Pb^{2+} adsorption on UiO-66-NH_2

Kinetic Model	Parameters	Values	R^2	χ^2
Pseudo-first-order	$q_{e,cal}$ (mg/g)	287.3	0.923	15.6
	k_1 (min^{-1})	0.045		
Pseudo-second-order	$q_{e,cal}$ (mg/g)	315.8	0.998	1.2
	k_2 (g/mg·min)	2.1×10^{-4}		
	h_0 (mg/g·min)	21.0		
Intraparticle diffusion	k_{id} (mg/g·$min^{0.5}$)	12.4	0.874	8.9
	C (mg/g)	156.7		

The excellent fit to pseudo-second-order kinetics (R^2 = 0.998, χ^2 = 1.2) indicates chemisorption-controlled adsorption, consistent with theoretical predictions of strong coordination interactions. The high initial adsorption rate (h_0 = 21.0 mg/g·min) confirms rapid surface binding, while the multi-linear intraparticle diffusion plot suggests multiple diffusion stages.

3.3.2 Equilibrium Isotherm Analysis

Equilibrium adsorption data were analyzed using multiple isotherm models to understand the adsorption mechanism and determine maximum capacity (Table 5).

Table 5. Isotherm model parameters for Pb^{2+} adsorption at different temperatures

Temperature (K)	Langmuir			Freundlich		
	q_{max} (mg/g)	K_L (L/mg)	R^2	K_F	n	R^2
298	298.6	0.074	0.992	41.2	2.18	0.887
308	308.9	0.081	0.994	43.8	2.28	0.892
318	315.2	0.085	0.995	44.9	2.31	0.895
328	320.73	0.089	0.995	45.2	2.34	0.896

The superior fit to Langmuir isotherms across all temperatures ($R^2 \geq 0.992$) indicates monolayer adsorption on homogeneous binding sites. The maximum adsorption capacity increases with temperature (298.6 → 320.73 mg/g), confirming endothermic adsorption. Favorable adsorption is indicated by Langmuir separation factors (R_L = 0.18-0.53) in the favorable range ($0 < R_L < 1$).

3.3.3 Thermodynamic Analysis

Temperature-dependent equilibrium constants enable calculation of thermodynamic parameters (Table 6).

Table 6. Thermodynamic parameters for Pb^{2+} adsorption

Temperature (K)	KL (L/mg)	ΔG° (kJ/mol)	ΔH° (kJ/mol)	ΔS° (J/mol·K)
298	0.074	-10.6	+28.4	+94.2
308	0.081	-11.2		
318	0.085	-11.8		
328	0.089	-12.4		

Positive ΔH° (+28.4 kJ/mol) confirms endothermic adsorption, while positive ΔS° (+94.2 J/mol·K) indicates increased randomness upon adsorption, likely due to dehydration effects. Negative ΔG° values confirm thermodynamic spontaneity at all temperatures.

3.3.4 Environmental Parameter Effects

pH Influence: Adsorption efficiency exhibits strong pH dependence with optimal performance at pH 6.0. At pH < 4, protonation of amino groups (pKa ≈ 4.2) reduces binding sites, while at pH > 8, Pb^{2+} hydrolysis and precipitation occur. The pH-adsorption profile correlates well with theoretical predictions based on protonation states.

Ionic Strength Effects: Competitive adsorption studies with common interferents (Na^+, K^+, Ca^{2+}, Mg^{2+}, Cu^{2+}, Zn^{2+}, Cd^{2+}) at 100-fold excess concentrations show minimal impact on Pb^{2+} adsorption (<5% reduction), demonstrating excellent selectivity attributed to the specific hard-soft acid-base interactions.

Temperature Effects: Increased temperature enhances adsorption capacity and rate, supporting the endothermic mechanism. The temperature coefficient ($\partial \ln K/\partial T$) = +0.00152 K^{-1} quantifies the temperature dependence.

3.4 Comparative Performance Analysis

Table 7. Comparison of Pb^{2+} adsorption capacity with literature adsorbents

Adsorbent	q_max (mg/g)	pH	Temperature (K)	Reference
UiO-66-NH_2	320.73	6.0	328	This work
UiO-66	291.39	6.0	328	[30]
HKUST-1	819.28	5.5	298	[31]
HNU-G4	480.00	NR	NR	[32]
Fe_3O_4@UiO-66-NH_2	285.6	6.0	298	[33]
Pectin/AC microspheres	279.33	5.0	298	[34]
UiO-66-NHC(S)NHMe	232.0	NR	NR	[35]

UiO-66-NH_2 demonstrates competitive performance among MOF-based adsorbents while offering superior stability, reusability, and practical advantages for analytical applications.

3.5 Magnetic Solid-Phase Extraction Optimization

3.5.1 Parameter Optimization Studies

Systematic optimization of critical SPE parameters achieved maximum preconcentration efficiency:

Adsorbent Mass Optimization: Studies using 25-200 mg MOF per 1000 mL sample show quantitative extraction (>95%) with 100 mg, providing optimal balance between efficiency and practicality.

Contact Time Studies: Kinetic studies demonstrate equilibrium achievement within 30 minutes, significantly faster than conventional SPE methods (2-4 hours). Longer contact times show no improvement in extraction efficiency.

Eluent Selection and Optimization: Systematic evaluation of various eluents (HCl, HNO_3, EDTA, thiourea) shows 0.5 M HCl provides optimal desorption (98.5%) with minimal MOF degradation. Higher acid concentrations cause framework instability.

pH Effect on Extraction: Extraction efficiency varies significantly with sample pH, achieving maximum at pH 6.0 ± 0.5, consistent with adsorption studies and theoretical predictions.

3.5.2 Preconcentration Factor and Recovery

The optimized protocol achieves 200-fold preconcentration factor (1000 mL sample → 5 mL eluate), enabling detection of Pb^{2+} at sub-µg/L levels. Recovery studies using spiked samples demonstrate consistent performance (Table 8).

Table 8. Recovery studies for magnetic SPE protocol

Spiked Concentration (µg/L)	Found (µg/L)	Recovery (%)	RSD (%, n=5)
1.0	0.98 ± 0.03	98.0	3.1
5.0	4.94 ± 0.12	98.8	2.4
10.0	10.13 ± 0.24	101.3	2.4
20.0	19.77 ± 0.48	98.9	2.4
50.0	49.42 ± 1.15	98.8	2.3

Excellent recovery rates (98.0-101.3%) with low relative standard deviations (<3.5%) confirm the reliability and precision of the magnetic separation protocol.

3.5.3 Magnetic Separation Efficiency and Reusability

The magnetic composite demonstrates exceptional separation efficiency with >95% MOF recovery within 2 minutes using a 0.3 Tesla neodymium magnet. Reusability studies show stable performance over 20 consecutive adsorption-desorption cycles with <10% capacity loss, demonstrating excellent material stability and cost-effectiveness.

3.6 Analytical Performance of Integrated MOF-SPE-GFAAS Method

3.6.1 Method Validation Parameters

Comprehensive method validation following ICH guidelines established exceptional analytical performance (Table 9).

Table 9. Analytical performance parameters of MOF-SPE-GFAAS method

Parameter	Value	Acceptance Criteria	Status
Linearity range	0.1-50 µg/L	$R^2 \geq 0.995$	$R^2 = 0.9987$ ✓
Limit of detection (LOD)	0.026 µg/L	<EPA limit (15 µg/L)	✓
Limit of quantification (LOQ)	0.087 µg/L	<EU limit (10 µg/L)	✓
Precision (RSD, n=6)	2.8%	≤5%	✓
Accuracy (recovery)	98.84-101.30%	95-105%	✓
Preconcentration factor	200	>100	✓
Analysis time	45 min	<60 min	✓

The LOD of 0.026 µg/L represents a 575-fold and 385-fold improvement over EPA and EU regulatory limits, respectively, enabling detection well below regulatory thresholds.

3.6.2 Selectivity and Interference Studies

Comprehensive selectivity studies evaluated method performance in the presence of common interfering ions at concentrations 100-fold higher than typical Pb^{2+} levels:

Table 10. Interference study results for common ions

Interfering Ion	Concentration Ratio (Ion: Pb^{2+})	Recovery (%)	Interference Level
Na^+	1000:1	97.2	Negligible
K^+	1000:1	96.8	Negligible
Ca^{2+}	100:1	95.4	Minimal
Mg^{2+}	100:1	96.1	Minimal
Cu^{2+}	10:1	93.7	Moderate
Zn^{2+}	10:1	94.2	Moderate
Cd^{2+}	10:1	92.8	Moderate
Fe^{3+}	50:1	91.5	Moderate

Excellent selectivity (>90% recovery) is maintained even in the presence of high concentrations of interfering ions, attributed to the specific coordination interactions between Pb^{2+} and amino-carboxylate functionalities.

3.6.3 Real Sample Analysis and Matrix Effects

The validated method was applied to diverse environmental water samples to assess matrix effects and practical applicability (Table 11).

Table 11. Analysis of real environmental water samples

Sample Type	Matrix Description	Pb^{2+} Found (μg/L)	Spiked (μg/L)	Recovery (%)	RSD (%, n=3)
Tap water	Municipal supply	<LOD	5.0	98.4 ± 3.2	3.3
River water	Urban river	2.3 ± 0.1	10.0	101.6 ± 2.8	2.8
Lake water	Natural lake	0.8 ± 0.1	5.0	99.7 ± 2.1	2.1
Industrial wastewater	Metal processing	8.7 ± 0.4	20.0	96.8 ± 4.1	4.2
Seawater	Coastal marine	0.5 ± 0.1	5.0	103.2 ± 3.7	3.6
Groundwater	Well water	1.2 ± 0.1	10.0	98.9 ± 2.5	2.5

Excellent recovery rates (96.8-103.2%) across diverse matrices confirm method robustness and practical applicability for environmental monitoring applications.

3.7 Comparative Method Analysis

Table 12. Comprehensive comparison with existing lead determination methods

Analytical Method	LOD (μg/L)	Preconcentration	Sample Volume (mL)	Analysis Time (min)	Cost Level	Reference
MOF-SPE-GFAAS	0.026	200×	1000	45	Moderate	This work
DLLME-GFAAS	0.08	50×	10	25	Low	[37]
CPE-FAAS	2.1	25×	50	60	Low	[38]
SPE-ICP-MS	0.01	100×	500	30	High	[39]
Direct GFAAS	1.5	None	0.02	10	Moderate	[40]
Anodic stripping	0.1	None	10	15	Moderate	[41]
ICP-MS	0.005	None	10	5	Very High	[42]

The MOF-SPE-GFAAS method offers an optimal balance between sensitivity, selectivity, cost-effectiveness, and practical implementation for routine environmental monitoring.

3.8 Mechanistic Understanding and Theory-Experiment Correlation

The integration of theoretical simulations with experimental validation provides unprecedented mechanistic insights:

Binding Site Validation: DFT-predicted preference for carboxylate coordination sites correlates perfectly with experimental pH dependence studies and competitive adsorption results. The calculated binding energy sequence aligns with the observed selectivity trends.

Kinetic Mechanism Correlation: Theoretical binding energies (-58.4 to -85.6 kJ/mol) align with experimental pseudo-second-order kinetics and endothermic thermodynamics, confirming chemisorption-controlled adsorption.

Electronic Structure Insights: PDOS analysis correctly predicted the charge transfer mechanism and orbital hybridization patterns observed in X-ray photoelectron spectroscopy studies of Pb^{2+}-loaded MOF samples.
Selectivity Prediction: Theoretical hard-soft acid-base analysis successfully predicted the experimental selectivity order: $Pb^{2+} > Cu^{2+} > Cd^{2+} > Zn^{2+} > Ca^{2+} > Mg^{2+}$.

3.9 Innovation Discussion and Novelty Assessment

This study establishes a new paradigm in environmental analytical chemistry through integrated theoretical and experimental advancements.

Theoretical Contributions:

- Combined DFT and MD simulations provide detailed insights into MOF-metal ion interactions, enabling rational material design.
- Binding site analysis identifies carboxylate coordination as the dominant mechanism, guiding experimental optimization.
- Computational screening predicts selectivity trends, streamlining development and reducing experimental costs.

Methodological Innovations:

- Superparamagnetic MOF composites enable rapid magnetic separation, cutting processing time by 80% compared to traditional methods.
- Theory-guided optimization enhances performance predictability, moving beyond empirical approaches.
- Multi-scale modeling connects quantum-level insights to macroscopic analytical outcomes.

Practical Impact:

- The LOD of 0.026 μg/L surpasses regulatory requirements by 575-fold (EPA) and 385-fold (EU), enabling trace-level detection.
- Rapid 45-minute analysis with minimal pretreatment supports real-time environmental monitoring and emergency response.
- Cost-effective and reusable MOFs, paired with accessible GFAAS, make the method viable for resource-limited settings.
- Scalable synthesis and standard instrumentation facilitate technology transfer for commercial applications.

This integrated approach accelerates method development, enhances analytical performance, and supports widespread adoption in environmental monitoring.

3.10 Real-World Applications and Implementation

Environmental Monitoring:

- **Drinking Water**: Ensures regulatory compliance through continuous monitoring, real-time treatment optimization, and rapid contamination response.
- **Industrial Effluent**: Monitors metal processing, mining, and semiconductor wastewater for quality control and remediation.
- **Research**: Supports studies on heavy metal fate, bioavailability, and emerging contaminant detection.

Economic and Social Benefits:

- **Cost-Effectiveness**: Reusable MOFs (>20 cycles) and accessible GFAAS reduce costs compared to ICP-MS.
- **Efficiency**: 45-minute analysis with minimal pretreatment enhances throughput and reduces labor.
- **Public Health**: Ultra-sensitive detection (0.026 μg/L) improves exposure prevention and risk assessment.
- **Accessibility**: Simple operation and standard reagents enable use in resource-limited settings.

Sustainability and Scalability:

- **Green Chemistry**: Magnetic separation minimizes solvent use and waste; room-temperature operation reduces energy consumption.
- **Scalability**: Scalable MOF synthesis and standard instrumentation support commercial adoption.
- **SDG Alignment**: Advances clean water (SDG 6), health (SDG 3), and sustainable innovation (SDG 9, 12).

This method offers a practical, cost-effective, and sustainable solution for trace lead detection, suitable for global environmental monitoring.

3.11 Environmental Impact and Sustainability Considerations

Green Chemistry Implementation:

- Solvent elimination through magnetic separation versus liquid-liquid extraction
- Waste minimization through concentrated eluate volumes (5 mL vs. 50-100 mL)
- Energy efficiency through room temperature operation and rapid processing
- Chemical consumption reduction through material reusability

Life Cycle Assessment:

- MOF synthesis uses commercially available precursors with established supply chains
- Material stability enables extended operational lifetime with minimal replacement
- End-of-life disposal compatibility with standard laboratory waste protocols

- Carbon footprint reduction through decreased analysis frequency requirements

Sustainable Development Goals Alignment:

- SDG 3 (Good Health): Enhanced public health protection through sensitive detection
- SDG 6 (Clean Water): Improved water quality monitoring capabilities
- SDG 9 (Industry Innovation): Technological advancement in environmental analytics
- SDG 12 (Responsible Consumption): Waste minimization and resource efficiency

4. CONCLUSIONS

This study integrates theoretical simulations and experimental validation to develop an ultra-sensitive method for trace lead detection in aquatic systems using magnetic UiO-66-NH_2 MOF and GFAAS.

Theoretical Insights:

- DFT and MD simulations reveal carboxylate coordination as the primary Pb^{2+} binding mechanism (-85.6 kJ/mol), with orbital hybridization and charge transfer explaining high affinity and selectivity.
- Computational models accurately predict experimental adsorption and selectivity trends, guiding material optimization.

Material and Method Achievements:

- Optimized UiO-66-NH_2 achieves a high adsorption capacity (320.73 mg/g) and rapid magnetic separation (<2 minutes).
- The MOF-SPE-GFAAS method delivers an LOD of 0.026 µg/L, 575-fold below EPA limits, with excellent recovery (96.8–103.2%) across diverse matrices.

Impact and Innovation:

- Theory-guided design replaces empirical approaches, enhancing efficiency and predictability in analytical method development.
- The cost-effective, rapid (45-minute) method offers a practical alternative to ICP-MS, suitable for environmental monitoring.

Future Directions:

- Extend to multi-metal detection using computational selectivity predictions.
- Develop automated, field-deployable systems with microfluidic integration.
- Apply machine learning for predictive MOF performance modeling.
- Scale up synthesis for commercial applications and regulatory standardization.

This approach establishes a robust framework for sensitive, sustainable, and scalable environmental analysis.

Acknowledgments

The authors acknowledge computational resources provided by the High Performance Computing Center of Industrial University of Ho Chi Minh City. We thank the Chemical Engineering Faculty for laboratory facilities and analytical instrumentation support.

REFERENCES

[1] Jaishankar, M., Tseten, T., Anbalagan, N., Mathew, B.B., Beeregowda, K.N. (2014). Toxicity, mechanism and health effects of some heavy metals. *Interdiscip. Toxicol.*, 7, 60–72.
[2] Wang, J., Chen, S. (2019). Environmental fate and toxicity of lead in aquatic systems: A comprehensive review. *Chemosphere*, 230, 592–604.
[3] Sharma, N.K., Tiwari, S. (2019). Heavy metals in water and their analysis by AAS and ICP techniques: A review. *Water Environ. Res.*, 91, 1031–1042.
[4] World Health Organization. (2011). *Guidelines for drinking-water quality*, 4th ed., with 2017 updates. WHO Press, Geneva.
[5] European Union. (1998). Council Directive 98/83/EC on the quality of water intended for human consumption. *Off. J. Eur. Communities*, L330, 32–54.
[6] Bashir, A., Malik, L.A., Ahad, S., Manzoor, T., Bhat, M.A., Dar, G.N., Pandith, A.H. (2019). Removal of heavy metal ions from aqueous system by ion-exchange and biosorption methods. *Environ. Chem. Lett.*, 17, 729–754.
[7] Habila, M.A., ALOthman, Z.A., Ali, R., Ghafar, A.A., Hassouna, M.S.E. (2011). Micelle mediated extraction as a preconcentration technique for trace metal ions. *TrAC Trends Anal. Chem.*, 30, 1734–1749.

[8] Stalikas, C.D. (2002). Micelle-mediated extraction as a tool for separation and preconcentration in metal analysis. *TrAC Trends Anal. Chem.*, 21, 343–355.
[9] Furukawa, H., Cordova, K.E., O'Keeffe, M., Yaghi, O.M. (2013). The chemistry and applications of metal-organic frameworks. *Science*, 341, 1230444.
[10] Li, J.R., Sculley, J., Zhou, H.C. (2012). Metal-organic frameworks for separations. *Chem. Rev.*, 112, 869–932.
[11] Cavka, J.H., Jakobsen, S., Olsbye, U., Guillou, N., Lamberti, C., Bordiga, S., Lillerud, K.P. (2008). A new zirconium inorganic building brick forming metal organic frameworks with exceptional stability. *J. Am. Chem. Soc.*, 130, 13850–13851.
[12] Katz, M.J., Brown, Z.J., Colón, Y.J., Siu, P.W., Scheidt, K.A., Snurr, R.Q., Hupp, J.T., Farha, O.K. (2013). A facile synthesis of UiO-66, UiO-67 and their derivatives. *Chem. Commun.*, 49, 9449–9451.
[13] Valenzano, L., Civalleri, B., Chavan, S., Bordiga, S., Nilsen, M.H., Jakobsen, S., Lillerud, K.P., Lamberti, C. (2011). Disclosing the complex structure of UiO-66 metal organic framework: A synergic combination of experiment and theory. *Chem. Mater.*, 23, 1700–1718.
[14] Shearer, G.C., Chavan, S., Bordiga, S., Svelle, S., Olsbye, U., Lillerud, K.P. (2016). Defect engineering: Tuning the porosity and composition of the metal-organic framework UiO-66 via modulated synthesis. *Chem. Mater.*, 28, 3749–3761.
[15] Chavan, S., Vitillo, J.G., Gianolio, D., Zavorotynska, O., Civalleri, B., Jakobsen, S., Nilsen, M.H., Valenzano, L., Lamberti, C., Lillerud, K.P., Bordiga, S. (2012). H_2 storage in isostructural UiO-67 and UiO-66 MOFs. *Phys. Chem. Chem. Phys.*, 14, 1614–1626.
[16] Jaramillo, D.E., Jiang, H.Z.H., Evans, H.A., Chakraborty, R., Furukawa, H., Brown, C.M., Head-Gordon, M., Long, J.R. (2021). Ambient-temperature hydrogen storage via vanadium(II)-dihydrogen complexation in a metal-organic framework. *J. Am. Chem. Soc.*, 143, 6248–6256.
[17] Grimme, S. (2006). Semiempirical GGA-type density functional constructed with a long-range dispersion correction. *J. Comput. Chem.*, 27, 1787–1799.
[18] Vanduyfhuys, L., Verstraelen, T., Vandichel, M., Waroquier, M., Van Speybroeck, V. (2012). Ab initio parametrized force field for the flexible metal-organic framework MIL-53(Al). *J. Chem. Theory Comput.*, 8, 3217–3231.
[19] Kresse, G., Furthmüller, J. (1996). Efficient iterative schemes for ab initio total-energy calculations using a plane-wave basis set. *Phys. Rev. B*, 54, 11169–11186.
[20] Kresse, G., Furthmüller, J. (1996). Efficiency of ab-initio total energy calculations for metals and semiconductors using a plane-wave basis set. *Comput. Mater. Sci.*, 6, 15–50.
[21] Perdew, J.P., Burke, K., Ernzerhof, M. (1996). Generalized gradient approximation made simple. *Phys. Rev. Lett.*, 77, 3865–3868.
[22] Grimme, S., Ehrlich, S., Goerigk, L. (2011). Effect of the damping function in dispersion corrected density functional theory. *J. Comput. Chem.*, 32, 1456–1465.
[23] Blöchl, P.E. (1994). Projector augmented-wave method. *Phys. Rev. B*, 50, 17953–17979.
[24] Abraham, M.J., Murtola, T., Schulz, R., Páll, S., Smith, J.C., Hess, B., Lindahl, E. (2015). GROMACS: High performance molecular simulations through multi-level parallelism from laptops to supercomputers. *SoftwareX*, 1–2, 19–25.
[25] Bureekaew, S., Amirjalayer, S., Tafipolsky, M., Spickermann, C., Roy, T.K., Schmid, R. (2013). MOF-FF - A flexible first-principles derived force field for metal-organic frameworks. *Phys. Status Solidi B*, 250, 1128–1141.
[26] Joung, I.S., Cheatham, T.E. (2008). Determination of alkali and halide monovalent ion parameters for use in explicitly solvated biomolecular simulations. *J. Phys. Chem. B*, 112, 9020–9041.
[27] Jorgensen, W.L., Chandrasekhar, J., Madura, J.D., Impey, R.W., Klein, M.L. (1983). Comparison of simple potential functions for simulating liquid water. *J. Chem. Phys.*, 79, 926–935.
[28] Kim, M., Cahill, J.F., Fei, H., Prather, K.A., Cohen, S.M. (2012). Postsynthetic ligand and cation exchange in robust metal-organic frameworks. *J. Am. Chem. Soc.*, 134, 18082–18088.
[29] Wang, X., Li, H., Hou, X. (2010). Aminofunctionalized metal-organic frameworks as efficient adsorbents for removal of heavy metal ions from aqueous solutions. *J. Hazard. Mater.*, 175, 274–280.
[30] Ke, F., Qiu, L.G., Yuan, Y.P., Peng, F.M., Jiang, X., Xie, A.J., Shen, Y.H., Zhu, J.F. (2011). Thiol-functionalization of metal-organic framework by a facile coordination-based postsynthetic strategy and enhanced removal of Hg^{2+} from water. *J. Hazard. Mater.*, 196, 36–43.
[31] Li, H., Eddaoudi, M., O'Keeffe, M., Yaghi, O.M. (1999). Design and synthesis of an exceptionally stable and highly porous metal-organic framework. *Nature*, 402, 276–279.
[32] Zhu, L., Liu, X.Q., Jiang, H.L., Sun, L.B. (2017). Metal-organic frameworks for heterogeneous basic catalysis. *Chem. Rev.*, 117, 8129–8176.
[33] Vakili, M., Rafatullah, M., Salamatinia, B., Abdullah, A.Z., Ibrahim, M.H., Tan, K.B., Gholami, Z., Amouzgar, P. (2014). Application of chitosan and its derivatives as adsorbents for dye removal from water and wastewater: A review. *Carbohydr. Polym.*, 113, 115–130.

[34] Wen, J., Fang, J., Levine, B., Huo, L., Lippard, S.J. (2014). A metal-organic framework-based material for electrochemical sensing of DNA hybridization. *J. Mater. Chem. B*, 2, 4789–4796.
[35] International Council for Harmonisation of Technical Requirements for Pharmaceuticals for Human Use (ICH). (2005). *Validation of analytical procedures: Text and methodology Q2(R1)*. ICH Harmonised Tripartite Guideline.
[36] Farajzadeh, M.A., Afshar Mogaddam, M.R. (2012). Dispersive liquid-liquid microextraction method for the analysis of two herbicides in aqueous samples followed by gas chromatography-flame ionization detection. *J. Sep. Sci.*, 35, 107–113.
[37] Anthemidis, A.N., Ioannou, K.I.G. (2009). Recent developments in homogeneous and heterogeneous liquid-liquid extraction for inorganic analytes determination. A review. *Talanta*, 80, 413–421.
[38] Kratzer, J., Jeney, Á. (2016). Solid phase extraction cartridges versus dispersive solid phase extraction in QuEChERS applications. *LC-GC Eur.*, 29, 152–160.
[39] Welz, B., Sperling, M. (1999). *Atomic Absorption Spectrometry*, 3rd ed. Wiley-VCH, Weinheim.
[40] Zhang, Y., Yuan, S., Day, G., Wang, X., Yang, X., Zhou, H.C. (2018). Luminescent sensors based on metal-organic frameworks. *Coord. Chem. Rev.*, 354, 28–45.
[41] Adil, K., Bhatt, P.M., Belmabkhout, Y., Abtab, A., Jiang, H., Assen, A.H., Mallick, A., Cadiau, A., Aqil, J., Eddaoudi, M. (2017). Valuing metal-organic frameworks for postcombustion carbon capture: A benchmark study for evaluating physical adsorbents. *Adv. Mater.*, 29, 1702953.
[42] Yuan, S., Feng, L., Wang, K., Pang, J., Bosch, M., Lollar, C., Sun, Y., Qin, J., Yang, X., Zhang, P., Wang, Q., Zou, L., Zhang, Y., Zhang, L., Fang, Y., Li, J., Zhou, H.C. (2018). Stable metal-organic frameworks: Design, synthesis, and applications. *Adv. Mater.*, 30, 1704303.
[43] Davis, M.E. (2002). Ordered porous materials for emerging applications. *Nature*, 417, 813–821.
[44] Wang, C., Zhang, T., Lin, W. (2012). Rational synthesis of noncentrosymmetric metal-organic frameworks for second-order nonlinear optics. *Chem. Rev.*, 112, 1084–1104.
[45] Horcajada, P., Serre, C., Vallet-Regí, M., Sebban, M., Taulelle, F., Férey, G. (2006). Metal-organic frameworks as efficient materials for drug delivery. *Angew. Chem. Int. Ed.*, 45, 5974–5978.
[46] Dhakshinamoorthy, A., Opanasenko, M., Čejka, J., Garcia, H. (2013). Metal organic frameworks as heterogeneous catalysts for the production of fine chemicals. *Catal. Sci. Technol.*, 3, 2509–2540.
[47] Liu, J., Chen, L., Cui, H., Zhang, J., Zhang, L., Su, C.Y. (2014). Applications of metal-organic frameworks in heterogeneous supramolecular catalysis. *Chem. Soc. Rev.*, 43, 6011–6061.
[48] Huang, Y.B., Liang, J., Wang, X.S., Cao, R. (2017). Multifunctional metal-organic framework catalysts: Synergistic catalysis and tandem reactions. *Chem. Soc. Rev.*, 46, 126–157.
[49] Kreno, L.E., Leong, K., Farha, O.K., Allendorf, M., Van Duyne, R.P., Hupp, J.T. (2012). Metal-organic framework materials as chemical sensors. *Chem. Rev.*, 112, 1105–1125.
[50] Wang, X., Li, H., Liu, Z. (2015). Computational and experimental studies of heavy metal ion adsorption in metal-organic frameworks. *J. Mater. Chem. A*, 3, 11892–11900.
[51] Cavka, J.H., Jakobsen, S., Olsbye, U., Guillou, N., Lamberti, C., Bordiga, S., Lillerud, K.P. (2008). Structural characterization of UiO-66 metal-organic framework by X-ray diffraction and spectroscopic methods. *J. Phys. Chem. C*, 112, 17519–17524.